High Aspect Ratio Plasmonic Nanostructures for Sensing Applications

Birgit Päivänranta,[†] Hannes Merbold,[‡] Reto Giannini,[§] Luca Büchi,[§] Sergey Gorelick,[†,⊥] Christian David,[†] Jörg F. Löffler,[§] Thomas Feurer,[‡] and Yasin Ekinci[†,§,*]

[†]Laboratory for Micro- and Nanotechnology, Paul Scherrer Institut, CH-5232 Villigen-PSI, Switzerland, [‡]Institute of Applied Physics, University of Bern, CH-3012 Bern, Switzerland, [§]Laboratory of Metal Physics and Technology, Department of Materials, ETH Zurich, CH-8093 Zurich, Switzerland, and [⊥]VTT Technical Research Centre of Finland, P.O. Box 1000, FIN-02044 Espoo, Finland

ABSTRACT We present an experimental and theoretical study of plasmonic modes in high aspect ratio nanostructures in the visible wavelength region and demonstrate their high performance for sensing applications. Ordered and well-defined plasmonic structures with various cross-sectional profiles and heights are obtained using a top-down fabrication process. We show that, compared to cylindrical nanorods, structures with split-ring resonator-like cross sections have great potential for powerful sensing due to a pronounced polarization dependence, strong field enhancement, structural tunability, and improved mechanical stability. The plasmonic structures under study exhibit high sensitivities, up to nearly 600 nm/RIU, and figures of merit above 20.

KEYWORDS: plasmonics · biosensing · nanofabrication · split-ring resonators · high aspect ratio

Sensing of gas, liquid, and chemical compounds has become increasingly important in a myriad of different fields of science and technology and has its applications in our everyday life. Among the wide range of available techniques, optical sensing is particularly advantageous due to label-free and non-invasive detection methods suitable for accurate substance recognition. Of particular interest are plasmonic chemical and biosensors which rely on the collective electron oscillations at metal–dielectric interfaces. These structures provide fast and reliable detection with very high sensitivities due to locally enhanced electric field densities.[1−5] In the simplest plasmonic sensing system, light impinging onto a thin conducting metal film triggers the propagation of resonant surface plasmons at frequencies that depend on the optical properties of the surrounding dielectric medium. Replacing the film with metallic nanostructures allows localization of the plasmon modes on the structure and tunability of the resonance frequency through adjustment of the nanoparticles' geometry.[3] Recent developments in nanoengineering methods, together with increased fundamental knowledge, have boosted research in the field of plasmonic (bio)sensing and generated more complex designs with increased sensitivities.[6] So far, the majority of studies report biosensing platforms based on shallow metal particles.[7−11] In recent years, however, high aspect ratio (AR) metallic nanostructures have been a topic of considerable interest which, compared to their shallow counterparts, show increased sensitivities due to the larger volumes of enhanced near-fields resulting from longitudinal plasmonic modes.[12−16] Especially, high AR cylindrical nanorods have been under study, which have been fabricated using bottom-up approaches such as chemical synthesis[17] or the use of alumina templates resulting in hexagonally packed arrays.[12,16] For better insight into the underlying physics of the high AR nanostructures' resonant behavior, and for achieving higher sensitivities, one should, however, be able to freely tailor their geometry. Accurate parametric design of well-ordered plasmonic nanostructures can only be realized using an optimized top-down lithographic fabrication process.

In this paper, we study arrays of high AR nanorods (NRs) with three different cross-sectional designs, as schematically illustrated in Figure 1. Starting with cylindrical nanorods (cNRs), we find that the sensing ability is determined by capacitive charging between the structures so that we continue by investigating nanorods with square cross sections (sNRs), due to their improved capacitive behavior. We further find that structures with asymmetric cross sections resembling split-ring resonators (SRRs) allow for even more promising bioplasmonic platforms due to an increased sensing performance, a strong polarization dependence allowing for difference spectroscopy, and improved mechanical stability. We exploit

* Address correspondence to yasin.ekinci@psi.ch.

Received for review April 26, 2011 and accepted July 11, 2011.

Published online July 11, 2011
10.1021/nn201529x

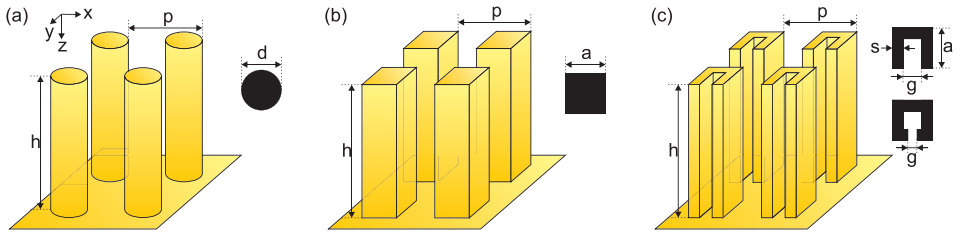

Figure 1. Schematic illustration of the high aspect ratio nanostructures with different cross-sectional designs under study. (a) Cylindrical nanorods (cNRs), (b) square nanorods (sNRs), and (c) split-ring resonators (SRRs) placed on a semi-infinite gold layer. The structural parameters are defined as h = height, p = period, d = cNR diameter, a = sNR side length, and g = SRR gap width.

our recently developed top-down fabrication method based on electron-beam lithography and gold electroplating[18] to manufacture arrays of plasmonic nanostructures with accurately defined structural parameters. The microscopic origins of the structures' resonant behavior are analyzed using numerical simulations, and their sensing abilities are investigated in experiments by varying the dielectric environment. The proposed metallic nanostructures may also show significant potential for various other plasmonic applications.[6,19,20]

RESULTS AND DISCUSSION

We start by considering the numerical response of cylindrical nanorods, as schematically shown in Figure 1a. The *E*, *H*, and *k* triad of the incoming light field is oriented along the *x*, *y*, and *z* axes, as illustrated in Figure 2a. In order to determine the microscopic origins of the resonances, we plot the distribution of the field enhancement (local electric field strength divided by incident electric field strength) along a line that is parallel to the nanorods' long axis and positioned 5 nm adjacent to the structure along the *x* axis, as indicated by the green line in Figure 2a. The field enhancement distributions obtained for 700 and 1000 nm high nanorods are shown in Figure 2b,c as a function of wavelength and *z* component. Here, the structures have a diameter of $d = 150$ nm and a periodicity of $p = 400$ nm. Within the wavelength interval considered, both structures exhibit two resonances that are marked by the dotted white lines. The plasmon resonances of nanorods correspond to longitudinal standing waves characterized by a node at the metallic base layer and an antinode at the rods' top end.[12] The nanorod response is composed of a series of standing waves of different order, where the number of nodes j along the height of the structure increases for decreasing wavelength. For the 700 nm high nanorods, the resonances observed correspond to the $j = 2$ and $j = 1$ modes, whereas for the 1000 nm high structures, they are assigned to the $j = 3$ and $j = 2$ modes, as indicated in Figure 2b,c. For a given free space wavelength λ_0, the structure height for which resonances occur can be estimated as

$$h = \frac{\lambda_0}{2n_{\mathrm{eff}}}\left(j + \frac{1}{2}\right) \qquad (1)$$

where n_{eff} denotes the effective refractive index. Using eq 1 and the Maxwell–Garnett theory[21] to determine n_{eff}, we calculate that the $j = 3$ and $j = 2$ resonances observed in Figure 2c should occur for structure heights of 932 and 925 nm, respectively. These values are somewhat lower than the assumed height of 1000 nm, which can be explained by the fact that the mode propagating longitudinally in the plasmonic structure is not perfectly reflected at the boundaries but experiences a phase change, which generates a smaller effective structure size.[22] The jth resonance translates into charge density maxima at $j + 1$ positions along the structure's long axis, where the charge concentrations induced by the incident field have opposite signs along the polarization direction. This is schematically illustrated in Figure 2a for the $j = 3$ resonance. Propagation of the plasmonic modes is defined by the cross-sectional geometry and in arrays is influenced by capacitive charging between neighboring rods. This results in a strong near-field dependence, as can be seen in Figure 2d, where we plot the field distribution in a *xy* slice, as marked by the light gray plane in Figure 2a. Between the nanorods, strong field values are obtained only in those regions where the rods face each other along a direction parallel to the incident field. For metallic structures, the frequency position of the resonances depends particularly strongly on the dielectric environment in regions of pronounced near-fields.[23] In terms of sensing applications, this means that the overall shift of the wavelength caused by a modification of the dielectric environment is greater when the volume of the high field strength region is as large as possible. Due to the circular shape of the nanorods, the highest field strengths are exhibited on the rod surface along the radial direction parallel to the polarization. The obvious approach to increase the sensing performance is therefore to use nanorods with square-shaped cross sections, as schematically shown in Figure 1b. Due to the parallel faces, sNRs act as larger capacitors where the high field strength regions comprise larger overall volumes. The field enhancement distribution in the proximity of such a structure is shown in Figure 3a. Here the structure height was $h = 1000$ nm, the side length was $a = 200$ nm, and the periodicity was set to

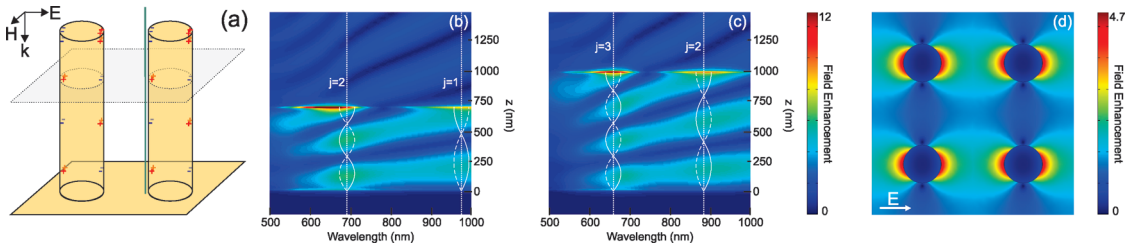

Figure 2. (a) Schematic illustration of the charge accumulations induced in 1000 nm high cNR arrays at the $j = 3$ resonance. Simulated field enhancement distribution along a line positioned 5 nm adjacent to (b) 700 nm and (c) 1000 nm high nanorods as indicated by the green line in (a). (d) Field enhancement distribution in the *xy* plane marked in (a) for $j = 3$ resonance at position $\lambda = 660$ nm .

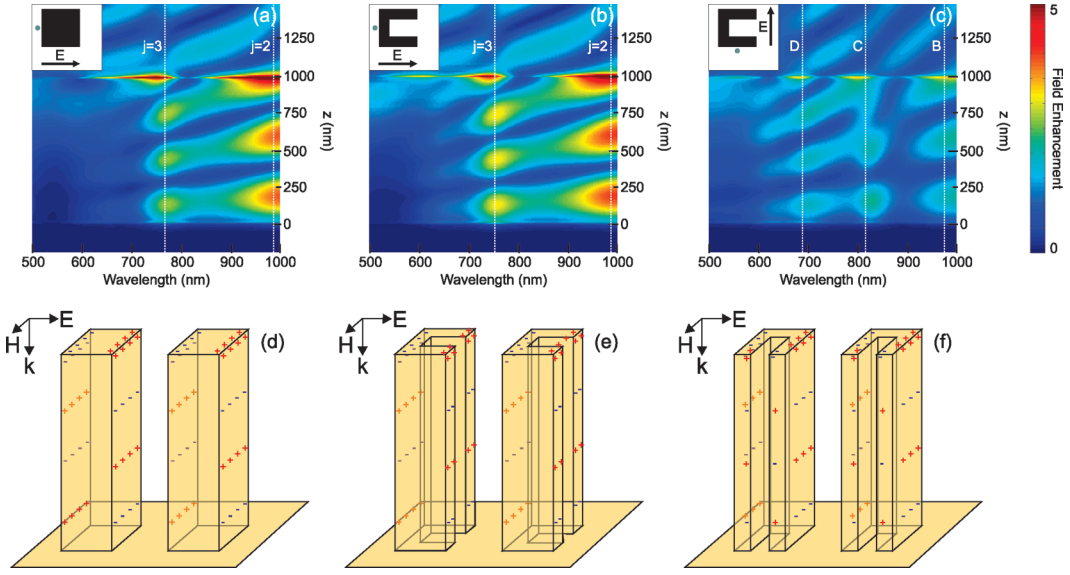

Figure 3. Simulated field enhancement distribution along a line positioned 5 nm adjacent to the high aspect ratio structures (green dot in insets): (a) sNRs, SRRs with 90 nm gap width under (b) *x*-polarization and (c) *y*-polarization. (d–f) Schematic illustration of the charge accumulations induced in the three nanostructures at the $j = 3$ resonance or *C* mode, respectively.

$p = 400$ nm. We again observe two resonances, which are attributed to the $j = 3$ and $j = 2$ modes, so that the field distribution obtained qualitatively resembles that of the 1000 nm high cNR structures (Figure 2c). We note that at the field enhancement sampled the chosen position in the sNRs is not as high as in the cNRs because the curved geometry of the cNR structures results in a strong localization of the charge carriers along the radial *x* direction. The induced charge carrier concentration in the sNRs, as obtained from the simulations, is schematically illustrated in Figure 3d for the $j = 3$ mode. As expected, neighboring sNRs act as parallel plate capacitors where the charges accumulate along the full length of the sNR faces parallel to the *y* axis.

We continue by investigating the response of a more sophisticated structure which features an asymmetric cross section resembling a split-ring resonator (SRR), as schematically shown in Figure 1c. We define our polarization directions so that *x*-polarization corresponds to the incident electric field as parallel to the SRR's gap-bearing side (SRR^x) and *y*-polarization corresponds to the electric field as perpendicular to the gap-bearing side (SRR^y). The field distribution adjacent to a SRR structure with $h = 1000$ nm, $a = 200$ nm, $p = 400$ nm, $s = 55$ nm, and $g = 90$ nm under *x*-polarization is shown in Figure 3b. Evidently, the introduction of the split has hardly any influence on the response, which can be understood by considering the $j = 3$ mode profile schematically illustrated in Figure 3e. The distribution of the charge accumulations is very similar to that exhibited by the square-shaped structures (Figure 3d), with the only difference that on the face containing the split the charge accumulations are slightly pushed together and concentrate on the two remaining face elements. This has no major influence on the underlying microscopic resonance mechanism of longitudinal standing waves and capacitive charging between neighboring elements. However, if the structures are illuminated by *y*-polarized light, a completely different behavior is obtained, as can be seen in Figure 3c, where three rather than two resonances are observed within the frequency range considered. The reason is that, for this orientation, the electric field can

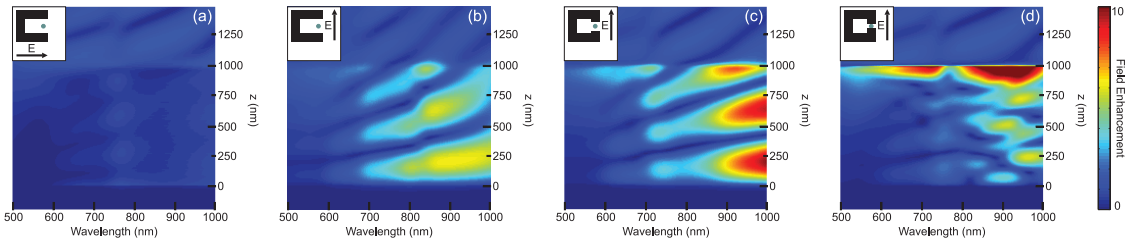

Figure 4. Simulated field enhancement distribution in the middle of the gap. (a) SRR under *x*-polarization with *g* = 90 nm and SRR under *y*-polarization with (b) *g* = 90 nm, (c) *g* = 50 nm, and (d) *g* = 10 nm.

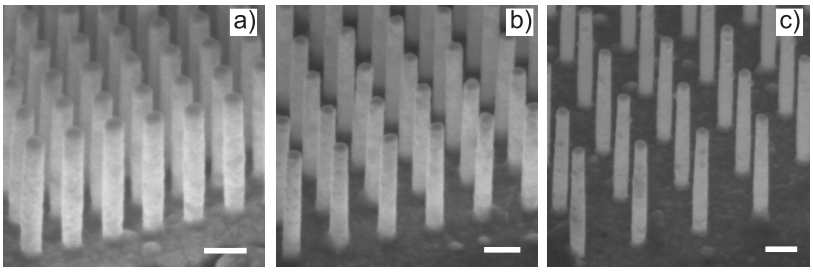

Figure 5. Scanning electron micrograph of fabricated cNRs with a height of *h* = 1000 nm and periodicities *p* and diameters *d* of (a) *p* = 200 nm and *d* = 100 nm, (b) *p* = 300 nm and *d* = 120 nm, and (c) *p* = 400 nm and *d* = 150 nm. The scale bar in all panels corresponds to 200 nm.

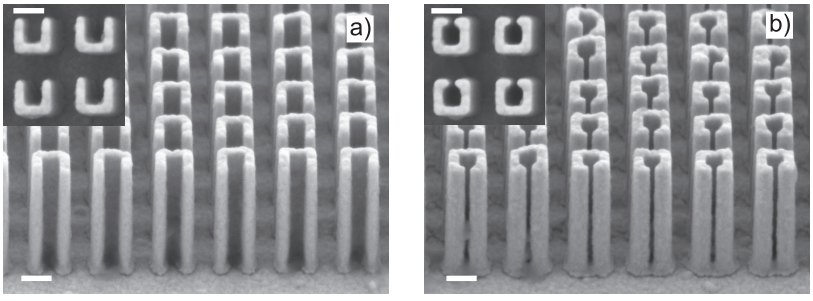

Figure 6. Scanning electron micrograph of fabricated SRRs with a height of 1000 nm and periodicity of 400 nm. The gap widths are (a) *g* = 110 nm and (b) *g* = 25 nm, and the scale bar in all panels corresponds to 200 nm.

also produce a capacitive charging across the gap within each individual SRR. The resulting resonances can therefore be considered as hybrid modes that are characterized by a superposition of in- and interstructure charging, as schematically shown in Figure 3f. The exact microscopic origins of the observed resonances are rather difficult to determine due to the complex three-dimensional geometry, which gives rise to longitudinal and in-plane current flows and results in admixtures of in- and interstructure charging. A detailed analysis of the underlying mechanisms will therefore be part of a future study. Since the mode hybridization renders the *j* notation inapplicable, the observed hybrid resonances are simply labeled *B*, *C*, and *D*. The fundamental resonance *A* appears at wavelengths larger than those considered here.

The field enhancement distributions in Figure 3a–c are plotted using the same color scale. Obviously, the obtainable field strength adjacent to the structure is smaller for SRRs under *y*-polarization than for *x*-polarization. This changes, however, if we consider the field enhancement distribution along a line positioned in midgap, as shown in Figure 4a,b. Whereas for the *x*-polarization case the gap is not charged, such that only very low in-gap field strengths are observed, the induced charging for *y*-polarization leads to strong and highly localized electric fields. The in-gap field distribution additionally exhibits a strong dependence on the gap width, as can be seen in Figure 4b–d. SRRs with narrower gap exhibit stronger near-fields inside the gap, which can be attributed to increased capacitive charging across the gap. However, a narrower split opening also means that the field can penetrate less efficiently into the gap, such that the field enhancement is shifted to the top end of the structure. Whereas for a gap width of *g* = 50 nm strong field enhancement is exhibited at three positions along the full length of the structure height, structures with *g* = 30 nm exhibit strong field enhancement only at two positions in the upper half of the structure (not shown here). For SRRs with even

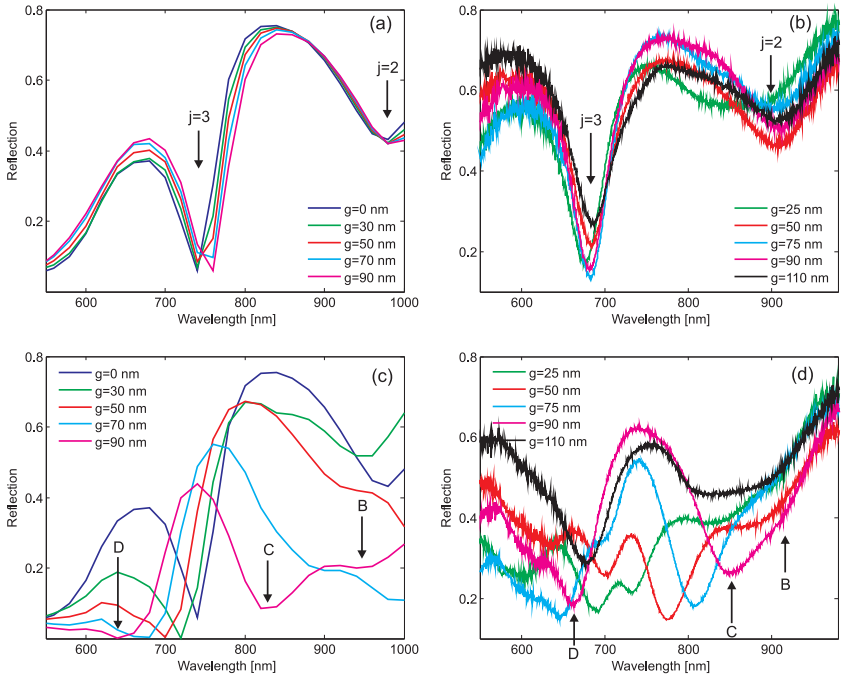

Figure 7. Simulated (a,c) and experimental (b,d) reflectance spectra for SRRs with heights h = 1000 nm, periodicity p = 400 nm, and varying gap widths, under x-polarization (top row) and y-polarization (bottom row).

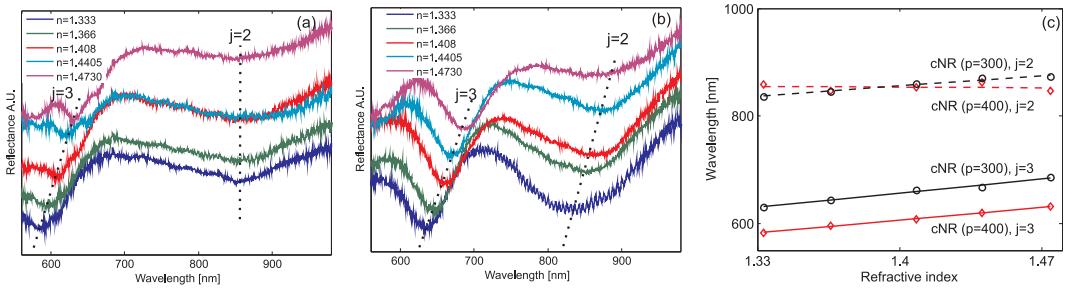

Figure 8. Reflectance spectra for different concentrations of aqueous glycerine solutions measured using high AR cNRs with a height of h = 700 nm: (a) cNRs with periodicity p = 400 nm and diameter d = 150 nm, (b) cNRs with periodicity p = 300 nm and diameter d = 120 nm. (c) Spectral resonance shift as a function of refractive index.

narrower gap (g = 10 nm), the field enhancement is localized at the structure's top end.

In order to verify the behavior predicted by the numerical simulations experimentally, we fabricated two sets of structures with cylindrical and asymmetric cross sections, respectively. The precise structuring at the nanoscale allowed us to fabricate a wide range of cNR structures of varying diameter and height, resulting in aspect ratios of up to 17 (height h = 1000 nm, diameter d = 60 nm). Figure 5 shows as examples three 1000 nm high cNR arrays with varying periodicities (p = 200−400 nm) and diameters (d = 100−150 nm). Since this fabrication technique allows us to tailor the cross-sectional geometry at will, we were also able to manufacture more complex high AR nanostructures with well-defined structure dimensions, such as the aforementioned asymmetric SRRs. Periodic SRR arrangements with structure heights of up to 1000 nm and highly vertical and smooth side walls were realized, as shown in Figure 6. The gap profile change can be seen in detail from the top-down images shown in the insets.

TABLE 1. Sensitivities of cNRs and SRRs for the Reflectance Minima Indicated in Figure 8, Figure 9, and Figure 10

		sensitivity (nm/RIU)						
type	height (nm)	j = 2	j = 3	j = 4	A*	B*	C*	D*
cNR^{400}	700	18	334					
cNR^{300}	700	183	376					
SRR^{x}	700	389	309					
SRR^{y}	700				490	425	335	
SRR^{x}	1000		598	392				
SRR^{y}	1000					540	510	425

Figure 7 shows the simulated and experimentally recorded reflectance spectra for the h = 1000 nm high SRR structures with varying gap width, fixed side wall

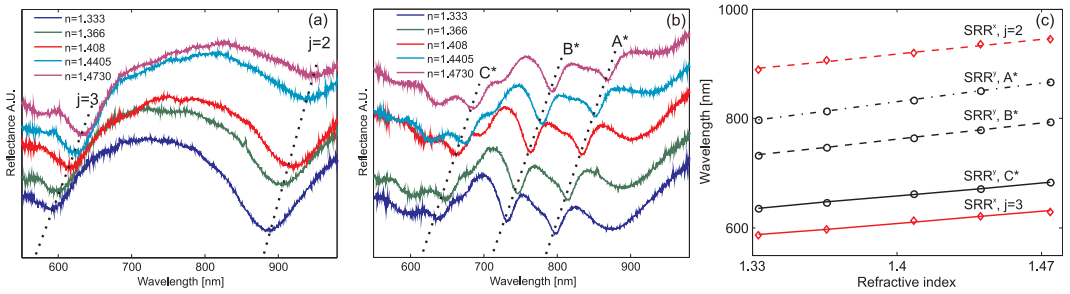

Figure 9. Reflectance spectra for different concentrations of aqueous glycerine measured using SRRs with heights of h = 700 nm, periods of p = 400 nm, and gap widths of g = 25 nm under (a) x-polarized and (b) y-polarized illumination. (c) Spectral resonance shift as a function of refractive index.

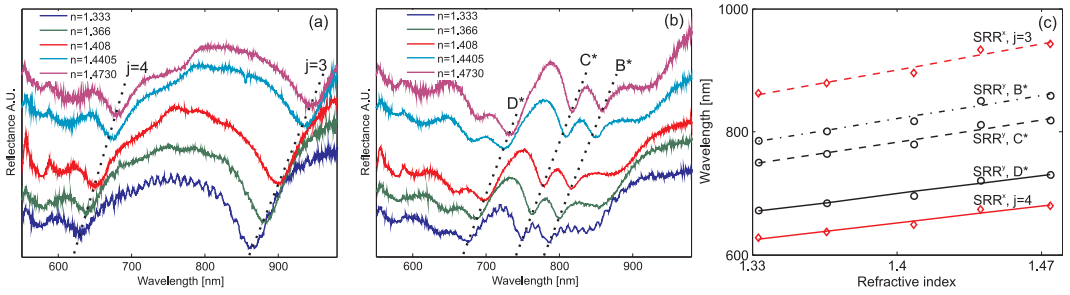

Figure 10. Reflectance spectra for different concentrations of aqueous glycerine measured using SRRs with heights of h = 1000 nm, periodicity of p = 400 nm, and a gap widths of g = 25 nm under (a) x-polarized and (b) y-polarized illumination. (c) Spectral resonance shift as a function of refractive index.

thickness s = 55 nm, and period p = 400 nm. The two resonances observed for SRRs under x-polarization (Figure 7a) correspond to the j = 3 and j = 2 modes, as indicated. In line with our previous findings, the gap is not charged for the incident polarization, so that the obtained spectra exhibit almost no dependence on the gap width. This behavior is also reproduced in the experimental spectra shown in Figure 7b. Good qualitative agreement is obtained between simulation and experiment, except that the measured resonances occur at slightly smaller wavelengths. This can be attributed to structural inaccuracies of the fabricated samples or to a deviation of the metal's dispersive properties from the values of a thin electroplated film. The corresponding reflectance spectra for the structures under y-polarization are shown in Figure 7c,d. As expected, a strong dependence on the gap width is observed, which is reproduced in both simulation and experiment. We note that some discrepancies are observed between the simulated and experimental spectra that are most likely linked to variations in the fabricated gap widths with respect to the simulation design. Whereas the gap widths between neighboring structures are comparable, the gap width within individual high AR SRRs along the z-direction is not constant due to limitations in the fabrication. Though it is not shown here, we observe that, for both incident polarizations, varying the side wall thickness between 45 and 60 nm has little impact on the spectral resonance positions.

We continued by investigating the structures' suitability for chemical or biological sensing applications by varying the refractive index (RI) of the medium surrounding the nanostructures. Figure 8 shows the spectral response of a square-packed cNR array with a height of h = 700 nm to different surrounding RI values. Two resonances are observed which are red-shifted if the refractive index n is increased. In comparison to cNRs in an ambient air environment (Figure 2b), the two resonances that occur within the frequency interval considered are therefore shifted by 1 order so that they are assigned to the j = 2 and j = 3 modes. Decreasing the periodicity from p = 400 nm (Figure 8a) to p = 300 nm (Figure 8b) verifies that a higher capacitance between the nanorods is beneficial due to larger wavelength shifts and more pronounced resonance peaks. Linear regression fits to the spectral resonance positions as a function of the RI change are shown in Figure 8c. The highest sensing sensitivities are obtained for the j = 3 mode, which yielded wavelength shifts of 334 and 376 nm/RIU for p = 400 and 300 nm, respectively. We note that these values are similar to sensitivities reported earlier for hexagonally packed high AR cylindrical nanorods.[12] For the j = 2 resonance, smaller wavelength shifts are observed; however, the improvement in the attainable sensitivity obtained upon reducing the periodicity is seen to be particularly strong. All sensitivities obtained for the resonances of the different structures considered here are summarized in Table 1. For 700 nm high SRRs,

the sensing performance was evaluated under the two incident polarizations. For SRR^x (Figure 9a), two resonance peaks are observed, which are again assigned to the $j = 3$ and $j = 2$ modes The corresponding sensing sensitivities are shown in Figure 9c, from which we determine wavelength shifts of 309 and 389 nm/RIU for the $j = 3$ and 2 modes, respectively. When the incident field is *y*-polarized (Figure 9b), we observe the emergence of three sharp dips in the reflectance spectra, which are again seen to shift toward larger wavelengths when the refractive index is increased. We note that an unambiguous assignment of these dips to the simulated modes for the structures in air (Figure 3c) would require a deeper theoretical understanding. For the liquid environment, we therefore use a notation where the three resonances are labeled as *A**, *B**, and *C**. The largest wavelength shift is obtained for hybrid resonance *A**, yielding a value of 490 nm/RIU, which shows that the parallel face elements enable improved sensing performance as compared to the cylindrical nanorods. We also note that, through a simple rotation of the incident polarization, we obtain a two-for-one resonance property where measurements under the polarizations can be combined using a difference spectroscopy approach[24] to obtain an improved signal-to-noise ratio. When the height of the cNR structures is increased to 1000 nm, we observe that the rods begin to be mechanically unstable due to capillary forces which arise during the drying of the solvent. We observed that the collapsing is proportional to the solvent surface tension. The sensing performance for the 1000 nm high cNRs could therefore not be evaluated reproducibly. For SRRs, on the other hand, this behavior is not observed due to the larger cross-sectional geometry, making them more robust and thus more suitable for sensing applications. Figure 10 illustrates the refractive index sensitivity and spectral resonance shift of the 1000 nm high SRR structures. Under *x*-polarization, the $j = 3$ and $j = 4$ modes are excited, whereas under *y*-polarization, the *B**, *C**, and *D** resonances are observed. For SRR^y, a maximum sensitivity of 540 nm/RIU is obtained for peak *B**, whereas for SRR^x, the $j = 3$ mode yields a record value of 598 nm/RIU, which is more than 110 nm/RIU higher than reported previously for other high aspect ratio structures or nanohole arrays.[5,12] The larger structure height results in a further increase of the sensing performance which can be explained by eq 1. An increased height *h* translates into a longer optical path at resonance wavelength, which contributes to easier detection of the absolute wavelength shift if the dielectric environment is modified.

To further verify the nanostructures' suitability for sensing applications, we evaluate the RI dependence in terms of a figure of merit (FOM) which additionally takes the sharpness of the resonances, that is, the full width at half-maximum (fwhm) of the peaks, into consideration. We use the definition introduced by Sherry *et al.*[25]

$$\mathrm{FOM} = \frac{m\ (\mathrm{eV\ RIU^{-1}})}{\mathrm{fwhm\ (eV)}} \qquad (2)$$

where *m* is the linear regression slope for the refractive index dependence and both *m* and fwhm are given in eV. These values facilitate a comparison of the sensing performance obtainable with different platforms. It should, however, be pointed out that the energy is reciprocally proportional to the wavelength, such that the dependence of the refractive index should only be approximated by a linear function for small changes of *n*. For nanorod arrays, the highest FOM values are obtained with a periodicity of $p = 300$ nm, where plasmon resonances with a fwhm of 0.3 eV (95 nm) lead to a FOM of 3.7. Similarly, a FOM of 3.5 is obtained for 700 nm high SRRs under *x*-polarization, whereas *y*-polarized illumination leads to a significantly higher FOM of 16.5, due to a combination of good refractive index sensitivity and narrow plasmon linewidths featuring a fwhm of 0.053 eV (30 nm). For the 1000 nm high SRR structures, *x*-polarized illumination results in an FOM of 6.5, whereas the highest overall figure of merit is obtained for *y*-polarization, reaching a value of 21.5, due to a fwhm as narrow as 0.046 eV (25 nm). The sensitivities and FOM values obtained here are among the highest reported at visible frequencies.[26]

CONCLUSION

In summary, we investigated the response of high AR nanostructures with various cross-sectional designs. Numerical simulations were used to elucidate the microscopic origins of the resonances and the consequential implications for the obtainable sensing performance. Using a novel fabrication process, tunable high AR cylindrical nanorods as well as more complex SRR-shaped nanostructures were fabricated, and their sensing abilities were experimentally investigated in the visible wavelength range. Our results showed that using asymmetric high AR structures offers various advantages over simpler cylindrical nanorods. In particular, a strong polarization dependence is exhibited, where one can switch between two completely different sets of modes *via* changing the incident polarization. For SRR^x, the response resembles that of square-shaped nanorods, whereas for SRR^y, hybrid resonances are excited that are characterized by a combination of in- and interstructure charging. The asymmetry therefore offers a powerful two-for-one property, in which the measurements performed under the two polarizations can be combined allowing for difference spectroscopy. This is a promising approach for further improvement of the sensing sensitivity, especially when combined with multivariate analysis. In addition, for SRR^y, the response exhibits a strong dependence on the gap width where a

narrower gap results in an increase of the in-gap field strength accompanied by a localization of the high field strength region to the upper surface of the structures. This can be utilized to realize structural tunability of the spectral resonance positions or to control the location of the high field strength region along the structure's long axis, which may be advantageous, for example, for optical data storage using tightly localized field intensities in multiplex writing at different wavelengths. The SRR structures were found to exhibit high mechanical stability, thus making them more robust particularly in liquid environment, where strong capillary forces are present. The mechanical robustness enabled fabrication of larger structure heights, which in turn led to further increase of the sensing performance. From the measurements, we determined refractive index sensitivities for the high AR SRRs, which ranged from 300 nm/RIU up to nearly 600 nm/RIU, with figures of merit reaching as high as 21.5 and surpassing those provided by nanorod arrays. Further studies are necessary for a detailed understanding of the plasmonic resonances of high AR SRR structures, which will also be beneficial for designing structures exhibiting even higher sensitivities. Our versatile fabrication technique based on electroplating would allow, in addition to gold, nanopatterning out of nickel which also possesses interesting plasmonic behavior.[27] Especially when combined with surface functionalization and device integration, complex-shaped high AR nanoplasmonic structures can show great potential for various biosensing applications. Finally, increasing the AR of plasmonic nanostructures can be useful for a variety of plasmonic applications, such as increasing the packaging density of plasmonic modulators by utilizing the vertical dimension and realizing novel plasmonic elements with a focus in optical applications.[28−30]

METHODS

Simulations. All numerical simulations in this study are based on the finite element method[31] using a commercial software package.[32] The modeling was carried out in the frequency domain, which allowed us to include the frequency-dependent properties of the metal structures using an extended Drude model which comprised critical point transitions.[33] The model parameters were obtained from a fit to the experimentally recorded refractive index data of the electroplated gold used in the fabrication. The refractive index of the surrounding dielectric was set to unity. For the simulations, the structures were positioned in the center of a box-shaped simulation domain together with a thick underlying Au layer. The thick Au layer enables us to assume a semi-infinite gold substrate and also acts as a seed layer during the fabrication process. The simulation domain was discretized using a tetrahedral mesh where the maximum element size was set to 100 nm in the dielectric and to 15 nm in the metallic regions. A plane harmonic wave was launched from the top boundary along the positive z axis, and the wavelength was scanned parametrically. The four boundaries perpendicular to the structure plane were set to periodic conditions, and the size of the simulation domain was chosen to represent the periodicity of the structures. For the two remaining boundaries, scattering boundary conditions were chosen in order to avoid unwanted reflections.

Fabrication. For the sample fabrication, we deposited a thick poly(methyl methacrylate) (PMMA) resist layer onto a gold-coated silicon substrate. The Au layer serves as a seed layer for a later electroplating step. The resist was patterned using a high-energy (100 keV) electron-beam writer and developed in high contrast developer solution of 3:7 H_2O/isopropyl alcohol. After development, the resist voids were filled with gold by electroplating, and the remaining polymer was subsequently removed by plasma ashing.[18]

Measurements. The reflectance spectra of the samples were recorded using an optical microscope (20× objective and NA = 0.4) couple to a spectrometer (range 500−1000 nm) with a cooled CCD camera and using a mercury lamp as a broad-band light source. For measurements in liquid environment, we applied aqueous glycerine solutions with different concentrations, which enabled us to change the ambient refractive index between 1.33 and 1.47. All of the reflection curves measured for the different nanostructures are referenced against the reflection of the flat underlying gold layer adjacent to the nanostructured region, and the refractive indices of the different solutions have been determined using an Abbe refractometer.

Acknowledgment. The authors thank A. Lehmuskero for ellipsometric measurements, A. Langner for discussions, and W. Wang for help with the measurements. Part of this work was funded by the Swiss National Science Foundation within the framework of the Nanotera program 20NAN1-123611 and projects 200020-119934 and 200021-125149.

REFERENCES AND NOTES

1. Homola, J. Present and Future of Surface Plasmon Resonance Biosensors. *Anal. Bioanal. Chem.* **2003**, *377*, 528–539.
2. Svedendahl, M.; Chen, S.; Dmitriev, A. Refractometric Sensing Using Propagating *versus* Localized Surface Plasmons: A Direct Comparison. *Nano Lett.* **2009**, *9*, 4428–4433.
3. Anker, J. N.; Hall, W. P.; Lyandres, O.; Shah, N. C.; Zhao, J.; Duyne, R. P. V. Biosensing with Plasmonic Nanosensors. *Nat. Mater.* **2008**, *7*, 442–453.
4. Yu, C.; Irudayaraj, J. Multiplex Biosensor Using Gold Nanorods. *Anal. Chem.* **2007**, *79*, 572–579.
5. Murray-Methot, M.-P.; Menegazzo, N.; Masson, J.-F. Analytical and Physical Optimization of Nanohole-Array Sensors Prepared by Modified Nanosphere Lithography. *Analyst* **2008**, *133*, 1714–1721.
6. Cai, W.; Shalaev, V. *Optical metamaterials*, 1st ed.; Springer: Berlin, 2010.
7. Félidj, N.; Aubard, J.; Lévi, G.; Krenn, J. R.; Schider, G.; Leitner, A.; Aussenegg, F. R. Enhanced Substrate-Induced Coupling in Two-Dimensional Gold Nanoparticle Arrays. *Phys. Rev. B* **2002**, *66*, 245407.
8. Koenderink, A. F. Plasmon Nanoparticle ArrayWaveguides for Single Photon and Single Plasmon Sources. *Nano Lett.* **2009**, *9*, 4228–4233.
9. Enkrich, C.; Wegener, M.; Linden, S.; Burger, S.; Zschiedrich, L.; Schmidt, F.; Zhou, J. F.; Koschny, T.; Soukoulis, C. M. Magnetic Metamaterials at Telecommunication and Visible Frequencies. *Phys. Rev. Lett.* **2005**, *95*, 203901.
10. McFarland, A. D.; Duyne, R. P. V. Single Silver Nanoparticles as Real-Time Optical Sensors with Zeptomole Sensitivity. *Nano Lett.* **2003**, *3*, 1057–1062.

11. Rockstuhl, C.; Zentgraf, T.; Guo, H.; Liu, N.; Etrich, C.; Loa, I.; Syassen, K.; Kuhl, J.; Lederer, F.; Giessen, H. Resonances of Split-Ring Resonator Metamaterials in the Near Infrared. *Appl. Phys. B: Laser Opt.* **2006**, *84*, 219–227.
12. Lyvers, D.; Moon, J.-M.; Kildishev, A. V.; Shalaev, V. M.; Wei, A. Gold Nanoarrays as Plasmonic Cavity Resonators. *ACS Nano* **2008**, *2*, 2569–2576.
13. Wurtz, G. A.; Dickson, W.; O'Connor, D.; Atkinson, R.; Hendren, W.; Evans, P.; Pollard, R. J.; Zayats, A. V. Guided Plasmonic Modes in Nanorod Assemblies: Strong Electromagnetic Coupling Regime. *Opt. Express* **2008**, *16*, 7460–7470.
14. Evans, P.; Hendren, W. R.; Atkinson, R.; Wurz, G. A.; Dickson, W.; Zayats, A. V.; Pollard, R. J. Growth and Properties of Gold and Nickel Nanorods in Thin Film Alumina. *Nanotechnology* **2006**, *17*, 5746–5753.
15. Kullock, R.; Graftsröm, S.; Evans, P. R.; Pollard, R. J.; Eng, L. M. Metallic Nanorod Arrays: Negative Refraction and Optical Properties Explained by Retarded Dipolar Interactions. *J. Opt. Soc. Am. B* **2010**, *27*, 1819–1827.
16. McPhillips, J.; Murphy, A.; Jonsson, M. P.; Hendren, W. R.; Atkinson, R.; Höök, F.; Zayats, A. V.; Pollard, R. J. High-Performance Biosensing Using Arrays of Plasmonic Nanotubes. *ACS Nano* **2010**, *4*, 2210–2216.
17. Huang, X.; Neretina, S.; El-Sayad, M. A. Gold Nanorods: from Synthesis and Properties to Biological and Biomedical Applications. *Adv. Mater.* **2009**, *21*, 4880–4910.
18. Gorelick, S.; Guzenko, V. A.; Vila-Comamala, J.; David, C. Direct E-Beam Writing of Dense and High Aspect Ratio Nanostructures in Thick Layers of PMMA for Electroplating. *Nanotechnology* **2010**, *21*, 295303.
19. Pendry, J. B. Negative Refraction Makes Perfect Lens. *Phys. Rev. Lett.* **2000**, *88*, 3966–3969.
20. Barnes, W. L.; Dereux, A.; Ebbesen, T. W. Surface Plasmon Subwavelength Optics. *Nature* **2003**, *424*, 824–830.
21. Maxwell Garnett, J. C. Colours in Metal Glasses, in Metallic Films, and in Metallic Solutions. II. *Philos. Trans. R. Soc. London* **1906**, *205*, 237–288.
22. Novotny, L. Effective Wavelength Scaling for Optical Antennas. *Phys. Rev. Lett.* **2007**, *98*, 266802.
23. Kafesaki, M.; Koschny, T.; Penciu, R. S.; Gundogdu, T. F.; Economou, E. N.; Soukoulis, C. M. Left-Handed Metamaterials: Detailed Numerical Studies of the Transmission Properties. *J. Opt. A: Pure Appl. Opt.* **2005**, *7*, S12–S22.
24. Weightman, P.; Martin, D. S.; Cole, R. J.; Farrell, T. Reflection Anisotropy Spectroscopy. *Rep. Prog. Phys.* **2005**, *68*, 1251–1341.
25. Sherry, L. J.; Chang, S.-H.; Schatz, G. C.; van Duyne, R. P.; Wiley, B. J.; Xia, Y. Localized Surface Plasmon Resonance Spectroscopy of Single Silver Nanocubes. *Nano Lett.* **2005**, *5*, 2034–2038.
26. Henzie, J.; Lee, M. H.; Odom, T. W. Multiscale Patterning of Plasmonic Metamaterials. *Nat. Nanotechnol.* **2007**, *2*, 549–554.
27. Chen, J.; Albella, P.; Pirzadeh, Z.; Alonso-González, P.; Huth, F.; Bonetti, S.; Bonanni, V.; Åkerman, J.; Nogués, J.; Vavassori, P.; *et al.* Plasmonic Nickel Nanoantennas. *Small* **2011**, DOI: 10.1002/smll.201100640.
28. Burgos, S. P.; deWaele, R.; Polman, A.; Atwater, H. A. A Single-LayerWide-Angle Negative-Index Metamaterial at Visible Frequencies. *Nat. Mater.* **2010**, *9*, 407–412.
29. Kawata, S.; Ono, A.; Verma, P. Subwavelength Colour Imaging with a Metallic Nanolens. *Nat. Photonics* **2008**, *2*, 438–442.
30. Verslegers, L.; Catrysse, P. B.; Yu, Z.; Shin, W.; Ruan, Z.; Fan, S. Phase Front Design with Metallic Pillar Arrays. *Opt. Lett.* **2010**, *35*, 844–846.
31. Jin, J. *The Finite Element Method in Electromagnetics*, 2nd ed.; Wiley-IEEE Press: New York, 2002.
32. *COMSOL Multiphysics 3.5*.
33. Etchegoin, P. G.; Le Ru, E. C.; Meyer, M. An Analytic Model for the Optical Properties of Gold. *J. Chem. Phys.* **2006**, *125*, 164705.